NanoScience
and Technology

S.V. Rotkin
S. Subramoney (Eds.)

Applied Physics of Carbon Nanotubes

Fundamentals of Theory, Optics and Transport Devices

Springer

11 Electrical and Mechanical Properties of Nanotubes Determined Using In-situ TEM Probes

J. Cumings and A. Zettl

In this chapter, we describe experiments performed on carbon and boron nitride nanotubes inside a transmission electron microscope (TEM). We demonstrate that it is possible to peel open the outer layers of a multiwall carbon nanotube to expose the inner shells. In this configuration, it is then possible to extract the inner shells in a telescopic extension mode. We present investigations of the forces associated with this extension and the electrical resistance of the nanotube during the telescoping process. We also described a series of studies of field emission and electrical conductivity using boron nitride nanotubes.

11.1 Introduction

11.1.1 Carbon and BN Nanotubes

Carbon nanotubes can be conceptually considered as originating from single-layer sheets of graphite, rolled up into perfectly seamless tubes with nanometer dimensions [1]. The sp^2 carbon-carbon covalent bond in graphite is among the strongest known bonds from chemistry, and carbon nanotubes therefore are mechanically robust. The bonds between layers of graphite, are relatively weaker Van der Waals bonds that give graphite its natural lubricating properties. Carbon nanotubes also have unique electronic properties, different from graphite, and present an exciting potential for nanoscale electronic devices.

The predominant synthesis methods for carbon nanotubes produce two distinct kinds of nanotube materials: single-wall nanotubes and multi-wall nanotubes. In a typical single-wall synthesis, the nanotubes vary in diameter from 1.0 nm to 1.4 nm, and can bond to one another in a regular parallel array on a triangular lattice. Such composite structures are sometimes referred to as ropes or bundles. A multi-wall nanotube, on the other hand, is a composite structure comprising many single-layer nanotubes, all nested concentrically. The spacing between the layers is close to the natural Van der Waals layer-layer spacing for graphite, 3.4 Å. Figure 11.1 shows transmission electron microscopy (TEM) images of single-wall and multi-wall carbon nanotubes.

Nanotubes can also be formed from other layered materials, notably boron nitride (BN) [3]. Boron and nitrogen lie to either side of carbon on the periodic table, and are the only other elements that can readily participate in

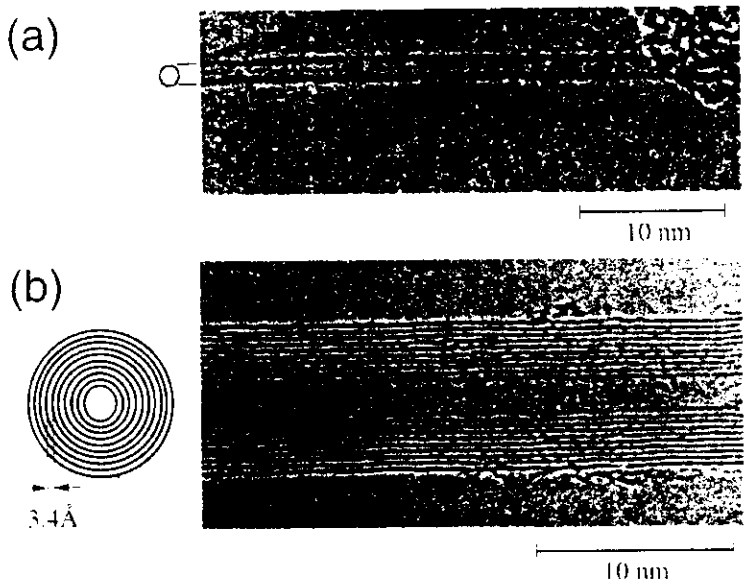

Fig. 11.1. Carbon nanotubes: (**a**) a typical single-wall nanotube; (**b**) a multi-wall nanotube [2]

sp^2 bonding. Bulk hexagonal boron nitride is a layered material analogous to graphite with similar structural properties [4]. The electronic properties, however, are markedly different. Due to the ionicity of the B–N bond, boron nitride has a bandgap of 5.8 eV in the graphitic phase [5]. Because of this, boron nitride nanotubes all have approximately the same bandgap (~ 5 eV) independent of the diameter or chirality of the nanotubes [6,7]. This could be useful for technological applications as opposed to carbon nanotubes which can be either metallic or semiconducting, depending on the structure. Figure 11.2 shows examples of single and multi-wall BN nanotubes, as examined by TEM. BN nanotubes are predicted to be more energetically stable structures that carbon nanotubes [8] and are expected to be more resistant to oxidation.

The virtually defect-free graphitic honeycomb network of carbon atoms of both single-wall carbon nanotubes and multi-wall carbon nanotubes suggests that various elastic moduli, such as the axial Young's modulus, might experimentally approach "ideal" graphite values. An early, but comprehensive overview of relevant theory is presented by Ruoff and Lorents [9]. Experiments bear out many of the theoretical predictions with axial Young's moduli of order 1 TPa being reported (see Table 11.1). A review of experimental results for carbon nanotubes is presented by Salvetat et al. [10].

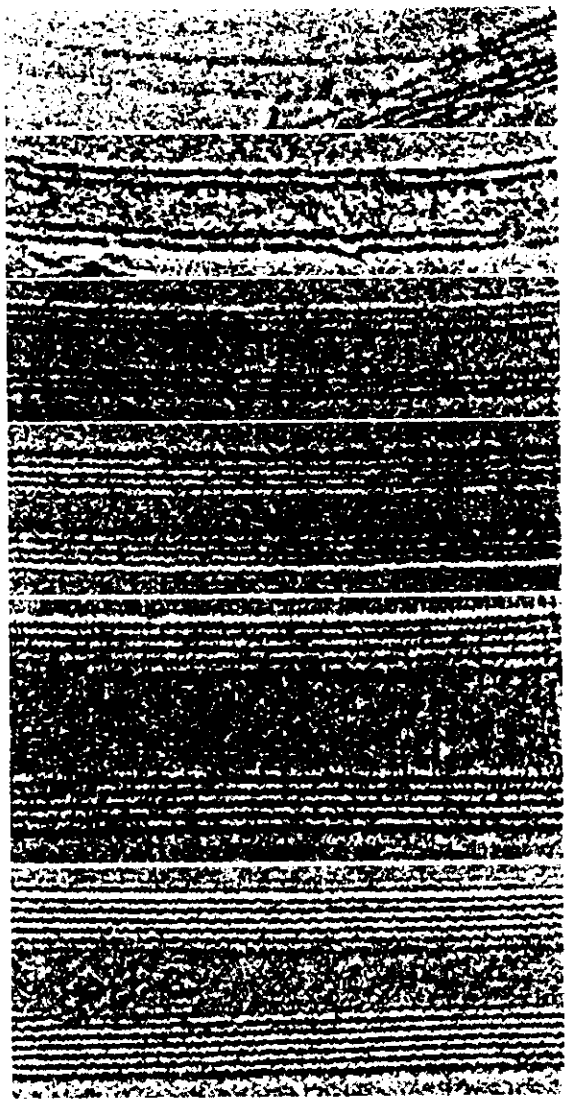

Fig. 11.2. TEM images of BN nanotubes (courtesy W.Q. Han)

There are several theoretical studies of the mechanical properties of non-carbon nanotubes. However, due to a paucity of good samples, there has only been one experimental investigation to our knowledge. The thermal vibrations of a boron nitride MWNT have been analyzed, and yield a Young's modulus of 1.22 ± 0.24 TPa [11].

The extremely high moduli and strengths for nanotubes, summarized in ble 11.1, suggest that they might make good mechanical elements on the noscale.

Table 11.1. Mechanical Properties of Nanotubes

	Material	SWNT	SWNT Rope	MWNT Arc-Grown	MWNT Chemically Grown	B–C–N Nanotubes
ung's odulus	Theoretical	~ 500 GPa [9]	0.4–0.8 TPa [12,13]	~ 1 TPa [12–14]		BN: ~ 0.9 TPa [15,16]
		~ 1 TPa [12,14,17,18]				BC_3: ~ 0.9 TPa [15,16]
		~ 350 GPa [19]				BC_2N: ~ 1.0 TPa [15,16]
		~ 1.2 TPa [15,16]				CN_x: ~ 0.6 TPa [16]
	Experimental	1.25 TPa [20]		1.8 TPa [21]	30 GPa [22]	BN: 1.22 TPa [11]
		~ 1 TPa [23]		1.2 TPa [24]	450 GPa [25]	
		2.8–3.6 TPa [26]		0.8 TPa [22]		
				0.1–1.2 TPa [27]		
				0.27–0.95 TPa [28]		
				1.7–2.4 TPa [26]		
ear odulus	Theoretical	~ 0.45 TPa [12,14,29]		~ 0.45 TPa [12,14]		
	Experimental		~ 1 GPa [23]			
nding rength	Theoretical	0.155 nm/d^2 Crit. Curvature [30]				
	Experimental			14 GPa [24]		
nsile rength	Theoretical	5–10% strain [31–34]				
	Experimental	> 45 GPa [35]	> 45 GPa [35]	11–63 GPa [28]	1–72 GPa [27]	

11.1.2 TEM Nanomanipulation

Nanomanipulationis a powerful tool. Atomic manipulation experiments using an STM (scanning tunneling microscope) have already demonstrated that nanomanipulation can facilitate the creation of atomic-scale structures that would be difficult to form or study by any other means [36–40]. The main problem with STM is that it requires a flat, conducting surface to work on. Furthermore, the process of acquiring an image of the surface requires scanning the STM tip back and forth many times, and can it can take several minutes just to acquire a single image. Atomic force microscopy (AFM) [41] and high-speed STM [42] lift some of these limitations, but the full benefits of nanomanipulation have yet to be realized. An alternative approach is to combine the manipulation capabilities of an STM, AFM, or related scanned probe with the imaging capabilities of high-resolution TEM. This allows continuous, real-time imaging during nanomanipulation on both conducting and insulating materials.

A nanomanipulation probe, in its simplest form, could simply be thought of as an STM tip. Instead of the location of the tip being controlled by a computer which maps out the surface, control of the position and voltage of the tip is given directly to the operator. It is possible, in principle, to modify surfaces, manipulate atoms, probe the mechanical and electronic properties of nanostructures, and build nanoscale mechanical and electronic systems. A number of such nanomanipulation stages have been developed for TEM applications [43–47]. The stages allow measurements to be carried out on delicate nanosystem geometries which are inherently unamenable to scanned probe techniques, all with real-time TEM imaging. This presents exciting opportunities for the study of physical properties of nanoscale systems, including nanotubes.

The biggest limitation to performing nanomanipulation experiments inside a TEM are the space constraints. The quality of the TEM magnetic lenses dictate the resolution of the microscope, and the highest quality lenses necessarily have the least room for samples inside. The objective lens comprises two conical anvils of magnet iron. The gap between the pole faces varies from microscope to microscope, but is typically about 2 mm. The specimen holder which loads the sample into the microscope can therefore only be about 1 mm in height. Mechanical vibrations can also present a problem for performing experiments inside a TEM, as small vibrations from room noise can completely blur out the atomic-scale features of a TEM image. Working within these constraint makes the design and construction of any custom TEM specimen stage a challenging task. The experiments described below were performed using a custom-built nanomanipulation stages, adapted to high-resolution TEM's.

1.2 Studies of Carbon Nanotubes

n order to perform measurements inside the TEM on individual nanotubes, it useful to have specimens from which nanotubes protrude in great numbers. n the case of carbon nanotubes, an easy source of such material is the soft ner boule material from a multiwall carbon nanotube arc synthesis [48]. his material contains many small fibers, and when one of these fibers is roken, the broken end has many pristine multiwall nanotubes protruding om it. It is also possible to process nanotubes into tangled mats, sometimes eferred to as "bucky paper" [49], and a torn edge of this bucky paper can lso be used for manipulation experiments.

Either the boule fibers or the bucky paper can be broken into pieces pproximately 50 µm by 500 µm. These pieces can be easily handled with weezers and attached to the manipulation setup. In a typical setup, the anotubes are glued in place with conductive adhesive. Sometimes a clean netal counter-electrode is used, and in this case a 50 µm-diameter gold wire erves nicely.

1.2.1 Electrically-Induced Mechanical Failure f Multiwall Carbon Nanotubes

Ve describe electrically-induced mechanical failure experiments performed t high bias on multiwall carbon nanotubes (MWNT's) inside the TEM. For hese experiments, MWNT were protruding from boule fibers glued to the TEM manipulation stage. The stationary electrode was a 50 µm-diameter old wire. The voltage was applied with a battery-powered voltage source, nd the current was monitored with a current amplifier. Both current and oltage were recorded on a computer-based 12-bit analog-to-digital acquisiion system.

Typical current-voltage characteristics for carbon MWNT's are shown in ig. 11.3. The top image shows the first voltage ramp after making contact o the nanotube. The initial resistance was 57 kΩ, which is a typical value. Several general properties of MWNT I-V curves are visible here. First, there is linear low-field region that is from 0.1 0.3 V wide, at bias values higher than his, the conductance typically increases, as can be seen from the nonlinearity n the I-V curve. At higher values still (above approximately 1.5 2.0 V), the onductance *decreases*, as can also be seen from the nonlinear I-V curve negative curvature). In the first plot in Fig. 11.3, the current voltage curve hows a non-reversible behavior: the conductance was decreased by increasing he voltage. This is a generic effect, and is apparently caused by current- and ield-induced annealing of the contact between the nanotube and the gold netal (or perhaps between the nanotube and its anchor in the boule fiber). Sometimes the annealing effect leads to a gradual change in the conductance as in the upper plot of Fig. 11.3) or to discrete jumps in the conductance (as

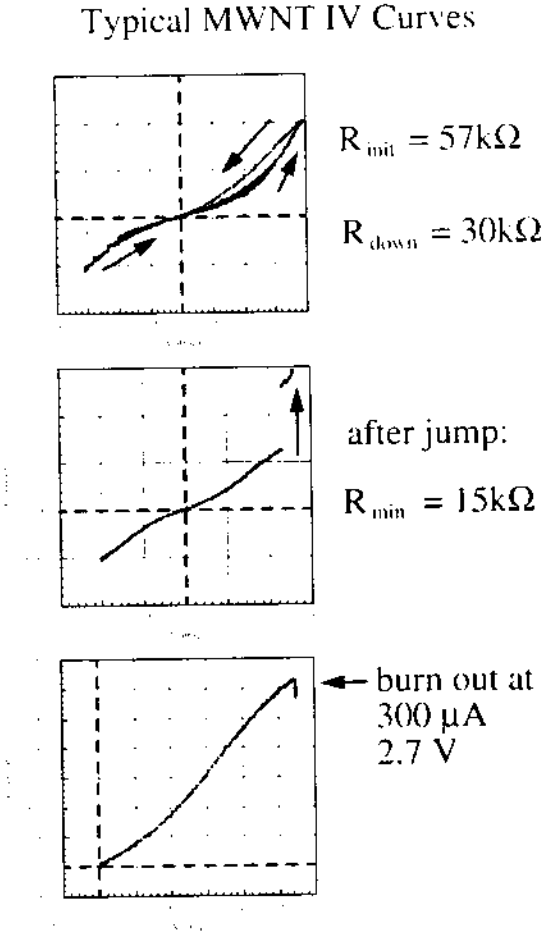

Fig. 11.3. Current-voltage curves taken on a carbon MWNT leading up to failure inside the TEM

in the middle plot of Fig. 11.3). After all annealing is completed, the nanotube from Fig. 11.3 has a low-bias resistance of 15 kΩ, which is typical.

This non-reversible annealing effect is *not* the cause of the nonlinear increase in current between 0.2 V and 1.5 V, as repeated curves through this region track this nonlinear behavior reversibly. This nonlinear effect could be due to conduction through more sub-bands in the nanotubes, or through a field-activated tunnelling phenomenon, such as tunnelling to inner nanotube shells [50], or hopping between localized states. The high-field nonlinearity above approximately 1.5 V (negative curvature) is probably associated with current saturation mechanisms in nanotube transport, and may be indicative

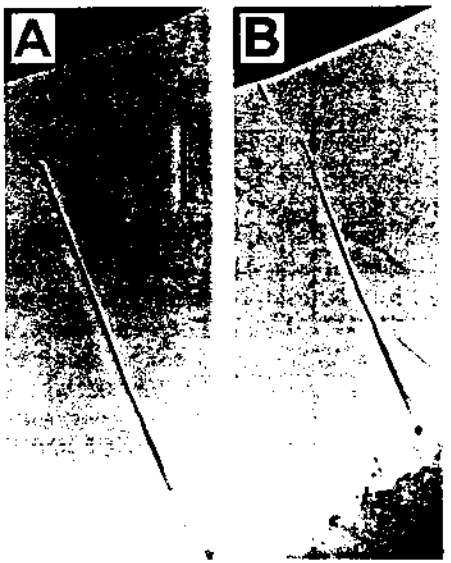

ig. 11.4. TEM images of a nanotube before (**a**) and after (**b**) electrical failure side a TEM. The scale bar (vertical in (**a**)) is 500 nm

f the onset of dissipative transport. In this region, we have observed effects hich suggest that the nanotubes are undergoing current-induced heating. hese are an increased motion (random walk) of carbon onions Van der Vaals bonded to the sides of the nanotubes, as well as the evaporation of etal beads deposited on the sidewalls of the nanotubes. This annealing effect as also led to a method for decreasing the contact resistance of nanotubes. ome nanotubes have considerable ($\sim$10 MΩ or greater) contact resistance hen initially contacted in the TEM by the gold electrode. If the nanotube connected in series with a current-limiting resistor of 1 MΩ or 100 kΩ, and he voltage is gradually increased to $\sim$5 V, the two-terminal resistance of the anotube decreases greatly, often coming into the range of 10–100 kΩ, or less.

At high biases, the nanotubes typically fail by forming a completely open rcuit, as shown in Fig. 11.4. Typical failure voltages are between 1.5 V and V, and typical failure currents are between 100 and 300 μA. During the ectrical failure, there is very little loss of carbon, unlike what is typically bserved for a macroscopic fuse. The details of the failure mechanism have een studied carefully elsewhere [50–52] in oxidizing environments, where ultiwall carbon nanotubes are observed to fail layer-by-layer. This failure ode is not observed in the present studies in the TEM, however, as the acuum prevents the controlled oxidation of nanotube layers. Instead, the anotube typically fails by a complete cleavage at some region near the middle f the nanotube. The cleaved ends of the nanotubes after failure often exhibit

a stepped, sharpened structure, suggesting that there is slightly more loss of carbon from the outer layers of the nanotube than from the inner layers. This is distinct from the peeling and sharpening effect, where only the outer layers are damaged, and the inner layers are left intact (described below).

11.2.2 Peeling and Sharpening Multiwall Carbon Nanotubes

Carbon nanotubes, due to their unique mechanical and electrical properties, are attractive candidates for a host of applications including catalysts [53], biological cell electrodes [54], nanoscale electronics [55,56], and scanned probe microscope and electron field emission tips [57,58]. For many such applications it would be desirable to control or shape nanotube geometry. For example, the "ideal" scanned probe, field emission, or biological electrode tip would be long, stiff and tapered for optimal mechanical response, and have an electrically conducting tip. Although recent progress has been made in the growth of nanotubes at pre-selected sites [59] and the modification of nanotube ends through chemical etching [60], finely-controlled nanotube shaping has not been possible.

A simple and reliable method has been developed that allows highly controlled engineering or shaping of multiwall carbon nanotubes (MWNT's) [61]. With this method average MWNT's are easily converted into "ideal-geometry" tips for scanned probe, field emission, or biological insertion applications. The shaping process involves electrically-driven vaporization of successive layers (i.e. tube walls) of the MWNT. Outer nanotube layers are successively removed near the end of the nanotube, leaving the core nanotube walls intact and protruding from the bulk of the MWNT. This peeling and sharpening process can be repeatedly applied to the same MWNT until the very innermost small-diameter tube or tubes protrude, often with a tip radius of curvature comparable to that of a single, single-walled nanotube.

The method has been demonstrated in a transmission electron microscope (TEM) configured with a custom-built mechanical/piezo manipulation stage with electrical feedthroughs to the sample. Figure 11.5 shows high resolution TEM images of a conventional arc-grown MWNT at different evolutionary stages in the peeling and sharpening process. The left end of the nanotube (not seen in the image) is attached to a stationary zero-potential gold electrode. To the right (also not shown) is a larger nanotube which serves as the "shaping electrode"; it is attached to the manipulator whose potential can be externally controlled. Figure 11.5a shows the MWNT in its pristine, as-grown state. For Fig. 11.5b, the shaping electrode has been momentarily brought into contact with the MWNT and a carbon onion has been inadvertently transferred from the shaping electrode to the MWNT, but the applied voltage (2.4 V) and current (170 μA) are below the shaping threshold and no peeling or sharpening has taken place. For Fig. 11.5c, the shaping electrode has been brought into contact with the tip of the MWNT at 2.9 V and 200 μA; numerous layers of the MWNT have been peeled away near its end and the

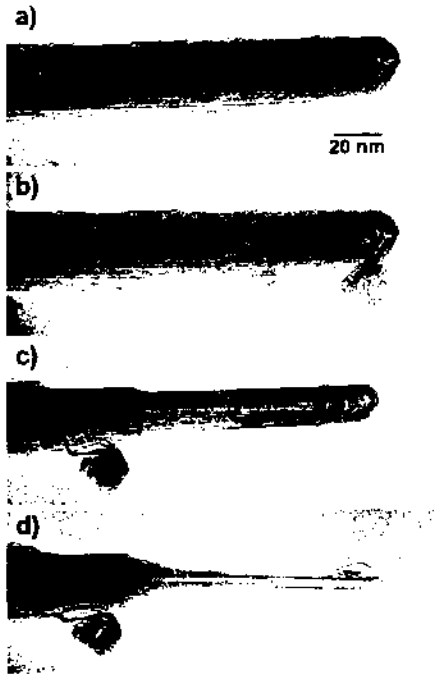

Fig. 11.5. Transmission electron microscope images of a multiwalled carbon nanotube being shaped: (**a**) the nanotube in its pristine form. It contains approximately 7 walls and has outer radius 12.6 nm; (**b**) a carbon onion has been inadvertently transferred to the nanotube end from the shaping electrode, but no attempt has been made to shape the nanotube; (**c**) & (**d**) the results of subsequent peeling and sharpening processes: the onion has simultaneously been displaced to a benign position down the tube axis. The shaped or "engineered" nanotube in (**d**) is thick and mechanically rigid along most of its length (not seen in the image) but tapers stepwise to a fine sharp (and electrically conducting) tip, ideal for scanned probe microscopy or electron field emission applications. The final long nanotube segment contains three walls and has outer radius 2.1 nm

MWNT now has a stepped diameter and is significantly sharpened. The carbon onion has been displaced to a benign position further down the tube. We note that the newly exposed tip of the MWNT appears undamaged. For Fig. 11.5d, the peeling and sharpening process has been repeated, resulting in a MWNT with highly desirable characteristics for many nanotube applications. The dominant protruding segment now consists of a three-walled electrically conducting nanotube with a radius of just 2.5 nm. We note that although we have used an in-situ TEM configuration to document the sharpening and peeling process, this is not a requirement. The process can be performed "blind" and monitored from the electrical characteristics of the

nanotube alone. In addition, the "shaping" electrode is easily replaced by a conventional conducting substrate.

This peeling and sharpening effect is distinct from the cleavage effect typically observed in electrical failure of nanotubes (see above). The peeling and sharpening is effected by using current-limiting on the voltage source (a 1 MΩ resistor), and bringing the manipulation tip briefly in contact with the nanotube at gradually larger and larger bias voltages. The peeling and sharpening is sometimes observed without current limiting only on extremely large diameter nanotubes (larger than ∼30 nm).

The physics behind the novel peeling and shaping process is intriguing. It appears improbable that uniform Joule heating of the nanotube would result in the observed behavior. It is more likely that MWNT's conduct ballistically [62], and the energy to break the carbon bonds and remove the MWNT layers originates from highly localized dissipation at defect scattering sites, located primarily at the ends of the tube. The fact that only the outer layers are affected suggests that electrical current in MWNT's flows primarily in just the outer carbon layers of the tube, consistent with the conclusions of recent MWNT magnetotransport experiments [63].

11.2.3 Telescoping Nanotubes: Linear Bearings and Variable Resistors

There is great current interest in shrinking the size scale of various mechanical systems, and dramatic recent advances have been achieved in the fabrication of microelectromechanical systems (MEMS) [64]. Ultimately, such systems are expected to reach well into the nanometer domain, and hence considerations of the mechanical behavior of materials at the nano- or atomic-scale, including those related to atomic perfection and friction, become critically important. Carbon nanotubes have unique mechanical [27, 65, 66] and electronic [67, 68] properties that make them outstanding candidates for nanomechanical or nanoelectromechanical applications.

In analogy to the well-known lubricating properties of Van der Waals bonded graphite, the individual cylinders of MWNT's might be expected to easily slide or rotate with respect to one another, forming near-ideal linear and rotational nanobearings. Recent theoretical calculations [69–71] indicate that the MWNT interlayer corrugation energy is indeed small, favoring such motion. For a MWNT, one could envision an extension mode much like the "telescoping" of a mariner's traditional spyglass. Some prior evidence for inadvertent MWNT telescopic extension can be found in severe mechanical stress failure mode studies, including MWNT's embedded in a stressed polymer composite [66] and for MWNT's torn apart in quasi-static tensile stress measurements performed in a scanning electron microscope [28]. Controlled and reversible telescoping of MWNT's has been more difficult to achieve.

A major difficulty in initiating controlled telescoping in MWNT's is the commonly capped ends which seal in all inner core nanotube cylinders. Even

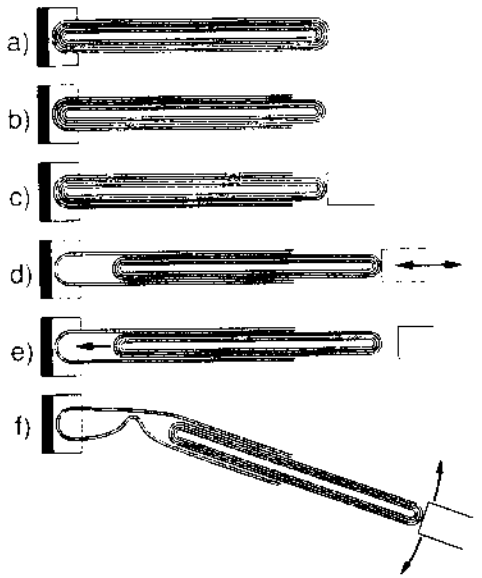

Fig. 11.6. A schematic representation of the experiments performed inside the TEM. Parts (**a**), (**b**), and (**c**) show the process of opening the end of a multiwall nanotube, exposing the core tubes, and attaching the nanomanipulator to the core tubes. Parts (**d**), (**e**) and (**f**) depict three different classes of subsequent experiments performed. In d) the nanotube is repeatedly telescoped, while observations for wear are performed. In (**e**), the core is released and pulled into the outer shell housing by the attractive Van der Waals force. In (**f**) lateral deflections of the nanomanipulator are performed to observe for kinking in the nanotube for different telescoped configurations

If the MWNT ends are opened by methods such as acid etching, it is difficult to selectively contact just the core tubes. One can exploit the peeling and sharpening technique described above to attach a moveable nanomanipulator [27] to only the core nanotubes within a MWNT. In-situ manipulation of the nanotube core allows controlled reversible telescoping to be achieved, and associated forces to be quantified. Robust ultra-low friction linear nanobearings and (constant-force) nanosprings are demonstrated. Mechanical nanotube failure modes, including reversible buckling and reversible collapse, are also investigated.

Figure 11.6 shows schematically the configurations used inside the TEM for the different mechanical experiments. An as-grown MWNT produced by conventional arc-plasma methods is first rigidly mounted (a), and the free end of the MWNT is then engineered to expose the core tubes (b). In (c) the nanomanipulator is brought into contact with the core tubes and, using electrical current, is spot-welded to the core. Figure 11.6c is the common

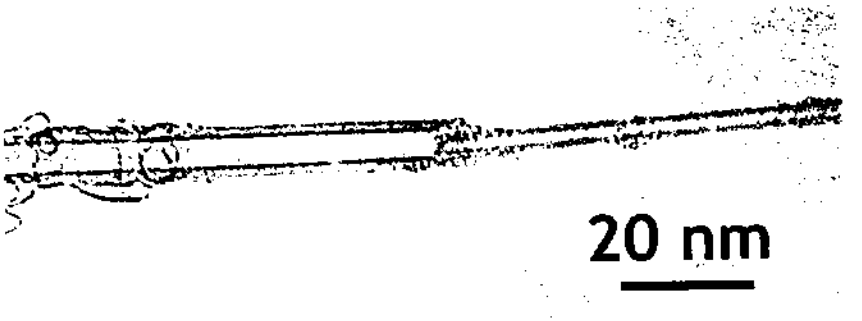

Fig. 11.7. A TEM image of a telescoped nanotube. This particular nanotube originally had 9 shells, but on telescoping a 4 shell core has been nearly completely extracted

starting point for all of the experiments to be described here. Sub-figures (d), (e), and (f) show three different classes of experiments. In d) the manipulator is moved right and left, thus telescoping the core out from, or reinserting it into, the outer housing of nanotube shells. The extration/reinsersion process can be repeated numerous times, all the while viewing the MWNT at high TEM resolution to test for atomic-scale nanotube surface wear and fatigue. In (e) the manipulator first telescopes out the inner core, then fully disengages, allowing the core to be drawn back into the outer shells by the intertube Van der Waals energy-lowering force. A real-time video recording of the core bundle dynamics gives information pertaining to Van der Waals and frictional forces. In (f), a partially-telescoped nanotube is subjected to additional transverse displacements, and reversible mechanical failure modes such as buckling and complete collapse are induced.

Figure 11.7 shows a TEM image of a MWNT in a fully telescoped position. Using higher resolution imaging than that used for Fig. 11.7, we determined that this MWNT originally had 9 walls, with an outer diameter of 8 nm and an inner diameter of 1.3 nm. After extension, a 4 nm diameter core segment (consisting of 4 concentric walls) has been almost completely extracted from the outer shell structure. The telescoping process was found to be fully reversible, in that the core could be completely pushed back into the outer shells, restoring the MWNT to its original "retracted" condition. The process of extending and retracting the core was repeated many times for several different MWNTs, and in all cases no apparent damage to the "sliding" surfaces, i.e. the outer tube of the core or the inner tube of the shell structure, was observed, even under the highest TEM resolution conditions ($\sim$2.5 Å). The apparent lack of induced defects or other structural changes in the nanotube contact surfaces at the atomic level suggests strongly that these near atomically-perfect nanotube structures may be wear-free and will not fatigue even after a very large number of cycles.

Telescoping Forces: A Linear Bearing

In the engineering of macroscopic bearings, the moving parts are typically cycled 10^3 to 10^6 times before definitive conclusions about wear can be drawn. This is because the damage from a single cycle is microscopic and cannot be readily observed by eye or even conventional microscopy. Here, atomic-scale imaging of the structure is possible and shows that after all cycles, from the first cycle onward, the atomic structure of the nanotubes is unaffected by the motion. Hence it is possible to conclude that the nanotube sections are near-perfect sliding surfaces, apparently free from wear for all cycles. Interestingly, in all MWNT's that we have examined, all repeated sliding motion for a given MWNT was observed to take place between the same two nanotube shells (and similarly no "multiple" telescoping was observed where the total length of the nanotube might become more than double the length of the original MWNT, as would occur from "sticking" of the segments at some point in their extension). We interpret this repeatability as a self-selection process where the most perfect surfaces offer the least resistance to motion. Importantly, even after repeated motions, the same surfaces remained the "most favored" ones, again providing evidence for no sliding-induced wear on the active surfaces. (Of course, in a many-walled MWNT, even the catastrophic failure (i.e. fusing) of one surface pair would not render the MWNT bearing unusable, as another (nearly equally perfect) surface pair would simply become the active elements). In some cases, there is a small amount of residual amorphous carbon produced during the initial core exposure process. Interestingly, because of the extremely small interwall clearance in MWNT's, such contamination appears to have no effect on the bearing action as it is simply brushed away upon reinsertion of the core section into the nanotube housing. Hence, MWNT-based linear bearings are self-cleaning and immune from typical contaminant-induced wear.

Several internal forces are associated with telescoping MWNT's. To first order these consist of the Van der Waals-derived force and possible static and dynamic frictional forces. The Van der Waals force is given by

$$F_{vdW} = -\nabla U(x) \tag{11.1}$$

where the Van der Waals energy [72] is given by $U(x) = 0.16Cx$ joules with C the circumference of the "active" nanotube bearing cylinders and x the length of the overlap between the core section and the outer walls, both measured in meters. The Van der Waals energy lowering gained by increasing the tube-tube contact area tends to retract the extended core of a telescoped MWNT. Interestingly, since the active intertube contact area decreases linearly with core tube extension, this restoring force is independent of contact area, or equivalently, independent of core extension. Hence, a telescoped nanotube with only one active (sliding) surface pair is expected to act as a *constant force* spring.

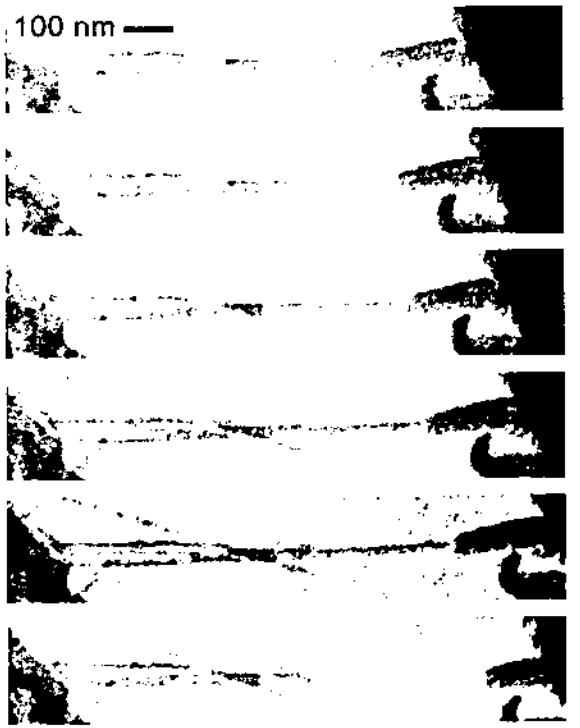

Fig. 11.8. Selected frames of a video recording of the in-situ telescoping of a multiwall nanotube. In the first five frames, the core nanotubes are slowly withdrawn to the right. In the sixth image, which occurred one video frame after the core was released, the core has fully retracted into the outer nanotube housing due to the attractive Van der Waals force

To determine experimentally if F_{vdW} dominates nanotube linear bearing dynamics we have used the configuration described in Fig. 11.6. The core tubes of a MWNT were first telescoped using the manipulator. Lateral deflections of the manipulator were used to fatigue and eventually break the spot weld, thus releasing the core segment. The resulting accelerated motion of the released core segment was recorded using a continuous video system tied to the TEM imaging electronics.

Figure 11.8 shows several selected frames from one such video recording. The upper five frames show the core segment being slowly and successively telescoped to the right (the structure in the left third of the image seen crossing the MWNT at about a 30° angle is another nanotube unrelated to the experiment and it is not in physical contact with the subject MWNT). Just after the fifth frame the manipulator has released the core segment. The sixth and final frame, which occurred one video frame after the release

of the nanotube, shows the core after it rapidly and fully retracted inside the outer shells of the MWNT. The dimensions for the core segment of the MWNT of Fig. 11.8 yield a core segment mass 2.9×10^{-16} g. Combining this with $C = 57$ nm and the initial extension of 330 nm, (11.1) leads to complete retraction of the core tubes in 4.6 nsec. This is at least consistent with the experimental observation that the complete contraction occurred in less than one video frame (33 msec).

From TEM observations, we may also draw conclusions about the static and dynamic friction between concentric shells of a multiwall nanotube. While macroscopic models of friction between solids dictate that friction is proportional to normal force, independent of contact area, modern microscopic models of friction predict that friction is in fact proportional to contact area [73]. In macroscopically rough samples, the actual contact occurs at point asperities, and the microscopic contact area is proportional to the total normal force. Nanotube shells, however, are atomically smooth, so any interlocking between the shells (due, for example, to the atomic corrugations) is best estimated by using the entire surface area of contact. The F_{vdW} retraction force for the nanotube in Fig. 11.8 is calculated to be a mere 9 nN. This indicates that the static friction force is small, with $f_s < 2.3 \times 10^{-14}$ Newtons-per-atom (6.6×10^{-15} Newtons-per-A^2). Furthermore, from the fact that the tube fully retracts, we conclude that the dynamic friction $f_k < 1.5 \times 10^{-14}$ Newtons-per-atom (4.3×10^{-15} Newtons-per-A^2). Friction is an important concern in small-scale systems, such as microelectromechanical systems, or MEMS [64], and recent atomic-scale frictional force measurements [74, 75] using conventional materials yield values approximately three orders of magnitude greater than the upper limit frictional forces found here for MWNT surfaces.

It is also possible to directly demonstrate through the images in Fig. 11.8 that the retraction force is, in fact, constant throughout the telescoping of the nanotube. The nanotube which was used as the anchor to spot weld to the tip of the core nanotube section was actually poorly anchored to the manipulator tip. It could be flexed in and out of the manipulator tip with a reasonable Hooke's law spring constant. By pushing this anchor up against a long nanotube, and using the known Young's modulus for MWNT [21], we estimated the spring constant for this nanotube deflection to be ~0.1 Newton-per-meter. In Fig. 11.9, we show the same images offset so that the manipulator tip (as noted by the kinked nanotube in the bottom right corner of each image) is at the same horizontal position in each frame. In these images it is possible to notice that the tip is at the same extension in each frame, implying that the retraction force is constant throughout the extension. We can also estimate the force from the spring constant to be ~5 nN, and we estimate that it is constant throughout the telescoping to within ±0.3 nano-Newton. Of course, the absolute accuracy of this order-of magnitude estimate is questionable, and is based on assumptions of linearity of the manipulator tip force response. The calculation is also subject to errors in the Young's modulus of the nanotube

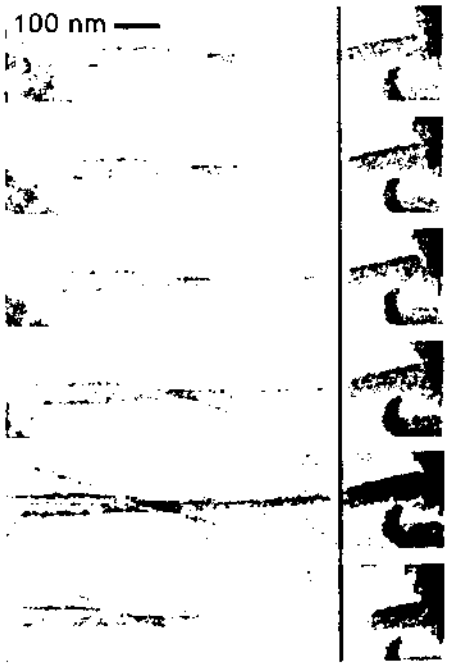

Fig. 11.9. The same images as Fig. 11.8. Here, the images have been offset to demonstrate that the anchoring nanotube, immediately to the right of the vertical line in the upper 5 images, feels a constant retraction force throughout the telescoping

used to calibrate it, but it is a good order-of-magnitude estimate of the retraction force. It also demonstrates the constancy of the retraction force, and the value agrees well with the calculations in the previous paragraph, which yield 9 nano-Newtons.

A note of interest is that if the (already generally small) friction between nanotube shells is indeed proportional to the length of the overlapping sections, then minimum bearing friction would be obtained for the shortest possible nanotube core/housing overlap. Several possibilities exist to achieve this configuration. First, a very short MWNT might be used from the outset. Second, the core of a long MWNT could be telescoped nearly all the way out, yielding a short contact area. The third possibility takes advantage of "bamboo" configurations [76] which sometimes occur in MWNTs, where the inner nanotube sections do not extend along the entire length of the MWNT, but rather represent an end-to-end series of shorter, fully capped, nanotube segments residing inside the continuous housing of outer nanotube shells. Figure 11.10a shows a close-up TEM image of such a bamboo joint inside a larger MWNT. In Fig. 11.10b, the core segment on the right has been telescoped

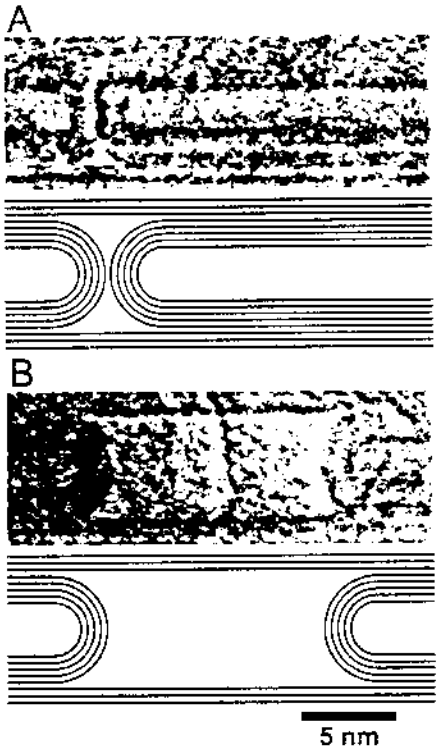

Fig. 11.10. TEM images of a bamboo section of a multiwall nanotube: (**a**) an as-grown bamboo section; (**b**) the same area after the core tubes on the right have been telescoped outward. Bamboo sections are independent and are free to slide inside their nanotube housing. The line drawings beneath the images are schematic representations to guide the eye

out, cleanly separating the bamboo joint. This is the first demonstration that bamboo nanotube core segments are truly independent sections with weak end-to-end binding. This observation has important practical implications for common-axis bearings: short independent bamboo sections might serve as ultra-low friction linear or rotational bearings that are firmly embedded in a common long, stiff cylindrical housing.

We now briefly consider lateral deformations of partially telescoped nanotubes. It has been predicted and observed that nanotubes can, upon lateral deformation, form kinks [65] or even fully collapse [77]. MWNT's with large inner diameters and few concentric shells are particularly susceptible to kinking and collapse. Although kinked or fully collapsed nanotubes have been observed experimentally using static TEM [65, 77] or atomic force microscopy methods [78], in-situ high-resolution controlled and reversible deformation

studies have been difficult. As outlined in Fig. 11.6f, using partially telescoped nanotubes we can study the kinking and collapse of a controlled nanotube system. We can directly alter the inner diameter and aspect ratio of the hollow nanotube, apply lateral forces, and in real time observe resulting failure modes. As expected, we find that a MWNT will kink and collapse much more readily after the inner core has been removed. One particular nanotube had 60 original layers with an outer diameter of 43 nm. A 40 layer core was telescoped out to a maximum extension of 150 nm, leaving an outer shell housing of just 20 layers with an inner diaster of 29 nm. The housing was supported at the base and the inner core section of the tube was still engaged in the housing for a length of 200 nm. When the manipulator was driven laterally to approximately $\sim 5^\circ$ angular displacement, the housing shells developed a kink in the middle of the large inner diameter section. At $\sim 26^\circ$ displacement the kink was severe and resembled the schematic in Fig. 11.6f. At any displacement angle, the telescoped core section was still mobile, and could be moved back and forth inside the unkinked portion of the outer shell housing. At small kink angles less than $\sim 10^\circ$, the core could be inserted past the kink position, forcing the kink to disappear and re-inflating the outer shells to their original circular cross section. At more severe bending angles, in excess of $\sim 20^\circ$, the kink blocked the inner core section from being fully inserted. Hence, suitable kinking of the outer shell housing provides an effective motion stop for nanotube core insertion.

The above results demonstrate that MWNT's hold great promise for nanomechanical or nanoelectromechanical systems (NEMS) applications. Low-friction low-wear nanobearings and nanosprings are essential ingredients in general NEMS technologies. The expected order 1–10 nsec transit time for complete nanotube core retraction implies the possibility of exceptionally fast electromechanical switches.

Telescoping Resistance: A Variable Resistor

The study of carbon nanotube electronic transport is an active experimental and theoretical research area. It has been demonstrated that single-walled carbon nanotubes (SWNT's) are physical realizations of ideal quantum wires with ballistic conduction [79–81]. Electronic conduction through multiwall carbon nanotubes (MWNT's), on the other hand, is complicated by inter-shell interactions and possible wavefunction interference between electronic states on different shells of the composite tube. For charge transport in such MWNT's the experimental understanding is complicated, with different studies variously supporting quantized electrical conductance, conductance dominated by transport along the outermost shell, diffusive scattering, and current-induced damage [52, 61–63, 80, 82–84]. Part of the difficulty is that most transport experiments are performed without detailed knowledge of the MWNT geometrical characteristics as might be obtained via high-resolution

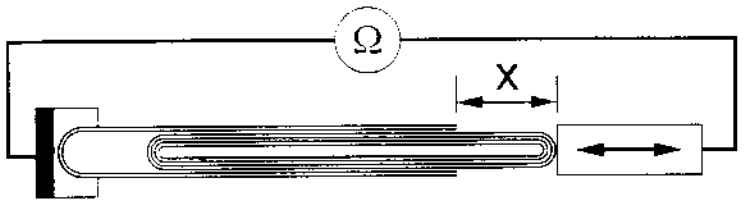

Fig. 11.11. Schematic diagram of telescoped MWNT resistance measurements. On the left is a nanotube anchored inside the TEM, and on the right is the manipulation tip. The nanotube is reversibly telescoped while the dc electrical resistance is measured with a low noise current amplifier

transmission electron microscopy (TEM). In addition, substrate or nanotube surface contamination effects may play a role.

Recently, it was demonstrated that the core shells of MWNT's could be controllably telescoped from their outer shell housings, thus constituting low-friction linear bearings [61, 85-87]. Such experiments were performed in-situ inside a high-resolution TEM, allowing simultaneous imaging of the MWNT system. An interesting measurement enabled by this geometry is the determination of the electrical resistance, R, between the ends of a telescoped MWNT as the telescoping distance, x, is varied. In this Letter, we report on the results of such measurements. For all nanotubes studied, R is found to increase nonlinearly with increasing x. The functional form of $R(x)$ and the electric field dependence of R are consistent with predictions for a one-dimensional localized system, with a room-temperature carrier localization length 1000–1500 nm. $R(x)$ is highly reproducible, suggesting that telescoped MWNT's constitute reliable high-resolution nanoscale rheostats.

The experimental starting point was MWNT's whose core tubes had been partially exposed and mechanically contacted using methods previously described [61, 85]. Briefly, one end of a bundle of surfactant-free (i.e. unprocessed) arc-grown MWNT's was embedded in silver paint and attached to a stationary electrode. The furthest protruding nanotube was peeled open and the protruding core tubes were contacted via spot welding to a piezo-driven nanomanipulator electrode. During the experiment, the dc electrical resistance between the two electrodes was monitored as the nanomanipulator (reversibly) telescoped the inner core tubes out from, or collapsed them back into, the outer nanotube housing.

Figure 11.11 shows schematically the experimental configuration. The telescoping or extraction distance x was monitored both via the nanomanipulator piezo drive voltages and analysis of direct TEM video recordings of the telescoping process. To aid in the analysis, each video frame contained critical data overlays. Throughout the telescoping process only one pair of adjacent concentric nanotube shells displayed relative motion, i.e. there was no multi-segment telescoping behavior. Typical MWNT initial (i.e. fully collapsed) lengths were from 1 to several microns. The nanotube system was always suspended in high vacuum inside the TEM (Topcon 002B, operating at 100 keV), thus eliminating potentially spurious substrate effects.

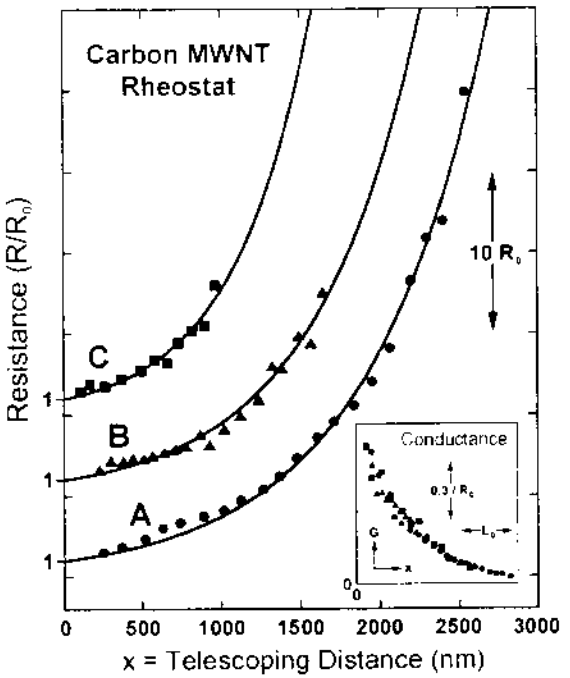

Fig. 11.12. Resistance R vs. telescoping distance, x, for three different nanotubes. The data are normalized to $R_0 = R(x \to 0)$. The inset shows the same data plotted as conductance $(1/R)$ as a function of normalized telescoping distance (x/L_0). Note that the conductance data are also nonlinear and collapse onto a universal curve

Figure 11.12 shows, for three independent MWNT's labeled A, B, and C, the resistance R between the ends of the telescoping nanotube system as a function of telescoping or core extraction distance x. The solid symbol data points have been normalized to R_0, the resistance of the $x \to 0$ unextended MWNT. The values of R_0 ranged from 3.5 kΩ to 110 kΩ. No extrinsic contact resistance is subtracted from the data we report here. Data such as those shown in Fig. 11.12 were recorded for successive extension and contraction runs and were found to be reproducible without evidence of significant hysteresis or temporal drift. The resistance data of Fig. 11.12 are clearly not linear in telescopic extension. To fit the data to a nonlinear functional form, we tentatively choose

$$R(x) = R_0 \exp\left(\frac{x}{L_0}\right), \tag{11.2}$$

with L_0 a characteristic length to which we attach a physical meaning below. The solid lines in Fig. 11.12 are fits of (11.2) to the three experimental $R(x)$ data sets. Fitting parameters for the three curves are given in Table 11.2, along with other relevant nanotube parameters obtained via TEM imaging, such as nanotube length and core and housing outer diameter. The inset of Fig. 11.12 shows the same data plotted as conductance, $G(x) = 1/R(x)$, as a function of the normalized telescoping distance, $x - L_0$; the conductance also exhibits nonlinearity with positive second derivative. From this observation and simple calculus manipulations we can rule out various functional forms for $R(x)$: any series combination of linearly changing resistance or conductance, any logarithmic dependence, or any power law, $R(x) \propto x^n$, where $n \leq 1$. Functional forms that are consistent with this observation include an exponential functional form, such as (11.2), or a power law with $n > 1$. We also note that in our telescoping experiments we have never observed conductance resonances or plateaus as might be expected from mercury-dipping experiments using non-telescoped MWNT's [62, 82, 83].

We now discuss these experimental findings. We first examine two candidate models for the resistance behavior: diffusive transport and junction tunneling. In the (semi-classical) diffusive transport model the increase in resistance with telescoping results from strictly geometric considerations. Two hollow and concentric, tightly fitting metal cylinders can show an increasing R that is not strictly linear with increasing telescoping distance x. Even assuming an isotropic conductivity tensor, this model is difficult to solve exactly, but in the limit of very thin cylinder walls or very long telescoping distances (as we have for the MWNT system), the model predicts a linear increase in R with increasing x. Under no circumstances does the generalized model yield the observed unique nonlinear length dependence.

In the junction tunneling model, the dominant contribution to the resistance arises from charge carriers tunneling from the telescoped nanotube core to the nanotube housing, while along the core and housing regions themselves the charge transport is assumed ballistic with no inherent length dependence to the resistance. A tunneling probability directly proportional to the core/housing overlap junction area then leads to a linear decrease in conductance, $1/R(x)$, with increasing x. This inset of Fig. 11.12 clearly shows that the conductance also decreases nonlinearly, ruling out this possible explanation. Indeed, our data suggest that the conductance of the sliding contact between the nanotube core and its housing is actually quite good, in agreement with independent experimental [50] and theoretical [88, 89] studies. The addition of a contact resistance to the junction tunneling model does not improve the fit to the experimental conductance data (this would cause a functional form with negative second derivative).

Table 11.2. The sizes of the nanotubes telescoped in this study, and the parameters extracted from the fits to the data shown in Fig. 11.12. The nanotube core section inner diameters are not given as they could not be unambiguously resolved from the microscopy images, but from observations of other nanotubes in our sample, the inner diameters are typically 1–3 nm. The R_0 and L_0 values are obtained by fitting the resistance data to (11.2).

Nanotube	Housing Outer Diameter	Core Outer Diameter	Core Length	R_0	L_0
A	25 nm	18 nm	2.6 μm	3.5 kΩ	760 nm
B	18 nm	7 nm	1.7 μm	54 kΩ	670 nm
C	20 nm	5 nm	1.1 μm	110 kΩ	490 nm

We propose that the correct interpretation of the observed nonlinear $R(x)$ is on-tube quantum interference and localization of electron wavefunctions similar to that first proposed by Landauer and Thouless for low-dimensional systems with defect scattering [90, 91]. In the original localization model, a conduction channel has a distribution of scattering sites, and the effect of increasing the length of the channel is to cause a linear increase in the number of scatters in the path of the transport current. Due to quantum interference, however, each scatter introduces a multiplicative factor in the averaged total system resistance, resulting in a resistance that increases exponentially with the length x of the system. The model also predicts an exponential dependence of resistance on temperature. While the signature of localization in the temperature dependence of resistance has been experimentally verified for a host of low-dimensional systems, including carbon nanotubes and graphitic materials [92–95], the unambiguous observation of an exponential length dependence of the resistance of a one-dimensional system has remained experimentally elusive[1].

The critical parameter in the localization model is the localization length l_c, representing the probability amplitude decay length of the (non-extended) electronic wavefunctions. For a two-terminal resistance measurement as employed for our telescoped MWNT system, the total resistance can be expressed within the localization model as [97][2]

$$R(x) = R_0 \exp\left(\frac{2x}{l_c} - 1\right) + R_c, \tag{11.3}$$

with R_c the resistance of the fully collapsed nanotube. With the substitutions $l_c = 2L_0$ and $R_0 = R_c$, (11.3) is in fact identical to (11.2). From our previous fits in Fig. 11.12 we find that the localization length l_c ranges approximately from 1000 nm to 1500 nm in the telescoped MWNT systems here investigated (see Table 11.2). The correspondence between the scaling factor

[1] This theoretical model has also been implicated in recent measurements of nonlinear resistance in single-walled nanotubes [96].

[2] Our experiments are performed at room temperature where conventional localization theory is applicable. At very low temperature, where electron correlation effects play a major role, (11.3) would require modification.

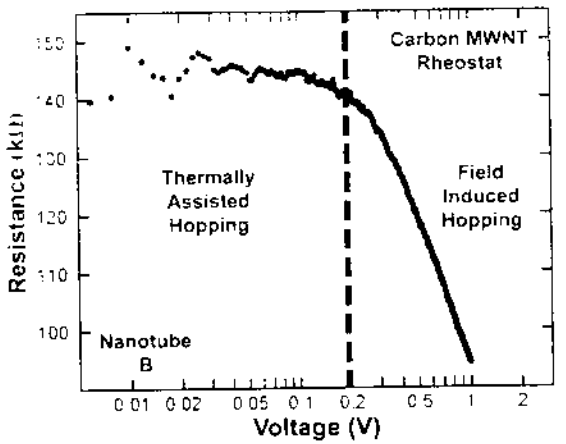

Fig. 11.13. Resistance vs. applied voltage of nanotube B when it is telescoped at a distance of $x = 580\,\mathrm{nm}$. The vertical *dashed line* is the calculated delineation between thermally-assisted carrier hopping and electric field assisted carrier hopping (see (11.4) and text)

R_0 and the collapsed tube "contact resistance" R_c suggests that R_c enters into the MWNT localization problem in the same way as do the intrinsic scattering sites, namely as a multiplicative factor.

Localization theory makes additional, experimentally testable predictions concerning the electric field E dependence of the electrical resistance [98]. For low applied E, ohmic conduction should be observed, while for high applied E the range of accessible states is increased leading to nonlinear conductance. The different field regimes can be characterized by the parameter [98]

$$\beta = \frac{eEl_e}{k_BT}. \tag{11.4}$$

where e is the electron charge, k_B is Boltzmann's constant, and T is the absolute temperature. For $\beta \ll 1$ transport is dominated by thermally-assisted hopping, while for $\beta \gg 1$ transport is dominated by field-induced hopping. We have measured the electric field dependence of the telescoped MWNT system, as shown in Fig. 11.13 for nanotube B at a fixed telescopic extension. At low applied voltages the resistance is approximately constant with some fluctuations due to experimental noise. At high applied voltages, however, the resistance decreases precipitously with increasing voltage. The vertical dashed line in Fig. 11.13 corresponds to $\beta = 1$, calculated using $l_e = 1340\,\mathrm{nm}$ as determined from the $R(x)$ fit for nanotube B. This demarcation agrees well with the observed transition from ohmic to strongly nonlinear resistance, providing additional support for carrier localization.

What is the origin of the "disorder" leading to carrier scattering and localization in the telescoped nanotube system? Some experiments have suggested that current through MWNT's flows almost exclusively on the outermost nanotube shell [63]. In a possible model, structural defects in this shell could then be a source of system disorder. In the present experiments, the outermost shell is not connected to both electrodes, but it is possible that the current flows in the outermost shell of the core segment until reaching the core–housing overlap, from which point current flows in the outermost shell of the housing segment. Thus, the effective length of the "outer" nanotube shell increases as the MWNT is telescoped. Alternatively, there is some evidence that even in non-overlapped regions of the nanotube, the transport current may probe more than one nanotube shell [50]. For typical nanotubes at room temperature, it has been suggested that approximately 3–7 shells contribute significantly to the current. Interlayer chirality mismatches can yield an effective disorder potential (analogous to that originally considered by Anderson) for the charges traversing the otherwise defect-free nanotube. Indeed, it has been demonstrated in theoretical studies that atomic mismatch between otherwise defect-free shells can lead to diffusive transport along the axis of MWNT's [99].

Our transport results have important implications for the degree of phase coherence for charge carriers in telescoped MWNT's. The nonlinear $R(x)$ behavior observed here implies that the carriers maintain a degree of phase coherence between scattering events, and that the phase coherence length $l_\phi \gtrsim l_e$. The exact relationship implied between the phase coherence length and the localization length is not clear, mainly because the regime of $l_\phi \sim l_e$ is not theoretically well understood [100]. An unambiguous exponential length dependence would be a clear sign of $l_\phi \gg l_e$. However, the data presented here do not unambiguously prove an exponential relationship. Such a proof typically demands data that vary over many decades. A general functional form of $R(x)$ is not known, to our knowledge, in the regime of $l_\phi \sim l_e$. The exponential form probably persists as l_ϕ is reduced, giving rise to other nonlinear forms for $l_\phi \sim l_e$ (such as a power law as suggested above for our data), then eventually to a linear form for $l_\phi \ll l_e$ (weak localization). However, even with conservative estimates, the phase coherence length is surprisingly long (perhaps as long as the nanotube itself), given that the experiments were performed at room temperature. The unique properties of nanotubes (including low concentrations of defects, weak electron–phonon coupling, and unusual Debye temperature and screening length [101–103]) are most likely responsible for the implied long l_ϕ values. This long phase coherence length observed here for MWNT's may have relevance to phase-coherent scanning tunneling microscopy, dual-tipped phase-coherent electron sources [104], or quantum computing systems.

From a nanoscale rheostat applications viewpoint, telescoped MWNT's have attractive mechanical and electrical characteristics. They may find util-

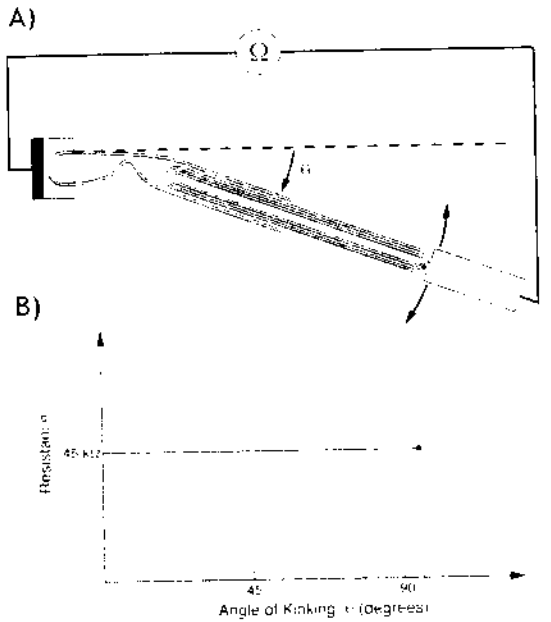

Fig. 11.14. Schematic of an experiment to measure resistance versus kinking for a MWNT

ity as tuning resistors, local strain gauges, or position sensors. Highly sensitive position encoders with nm-scale resolution have been previously developed [41, 105, 106], but in general those devices require large-scale detection systems making them impractical for efficient integration in self-contained nano-scale systems.

We now present a small set of preliminary studies on the resistance of MWNT studied as a function of bending and kinking. As shown schematically in Fig. 11.14A, a MWNT is first partially telescoped out, then lateral forces are applied to the ends of the core structure to induce controlled "kinking" in nanotube fabric. The kinking occurs in the large diameter "hollowed out" region of the tube, were the housing tubes are no longer supported by the inner core tubes. The kinking position can be controlled by varying the extension of the core tubes. All the while, the resistance between the ends of the tube is monitored. Figure 11.14B schematically shows the measured electrical resistance as the tube is kinked from its unperturbed straight configuration (θ=0°) to a severe right-angle kink (θ=90°). Surprisingly, no resistance changes are observed even for such extreme kinking. All kinking here performed was fully reversible, with no permanent tears in the nanotube fabric. Our findings suggest that even severely mechanically deformed nanotubes are good electrical conductors somewhat akin to flexible electro-

magnetic waveguides. It should be noted here that the bias on the nanotube and the gain on the current amplifier have been optimized to detect small changes in the resistance. Resistance changes as large as ~25% may not have been detected during the experiments reported here, and a more careful study of the effects of kinking on nanotube transport would be beneficial.

11.3 Studies of Boron Nitride Nanotubes

We describe field emission and contact current-voltage measurements on individual BN nanotubes. Figure 11.15 shows the setup for the measurements. The nanotubes were manipulated with a piezo-driven manipulation stage inside the TEM. The BN nanotubes are double-wall nanotubes synthesized by arc discharge [107], and purified by ultrasonic assisted filtration [108]. The as-purified BN nanotube samples are electrically insulating in bulk, but for the TEM in-situ measurements, the nanotubes were mixed with a conductive epoxy (Epo-Tek H20E) in a volume ratio of approximately 1:1. The resulting composite was then cleaved before loading into the TEM, and TEM imaging verified that clean nanotubes were protruding from the surface of the composite. The second electrode for the electrical measurements was a 50 μm gold wire. For field emission experiments, the tips of the protruding nanotubes were positioned 6 micron from the surface of the wire, and for contact IV measurements, the tips of individual nanotubes were gently brought into contact with the gold wire by the piezo manipulator. Control experiments were also performed to verify that the conductive epoxy itself does not field emit at the voltages applied in these experiments. The current was monitored in all cases with a high gain preamplifier.

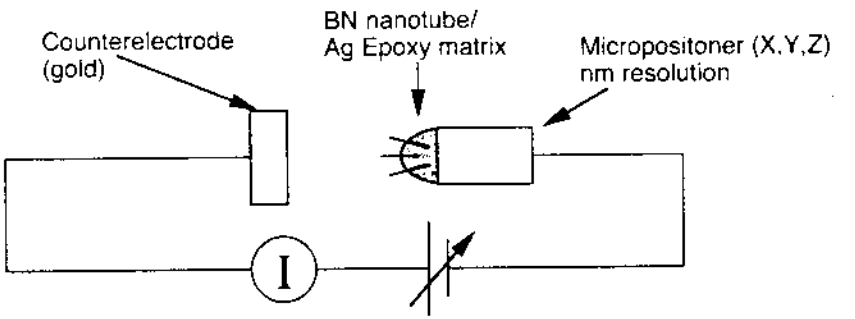

Fig. 11.15. The experimental setup for BN nanotube electrical measurements inside the TEM

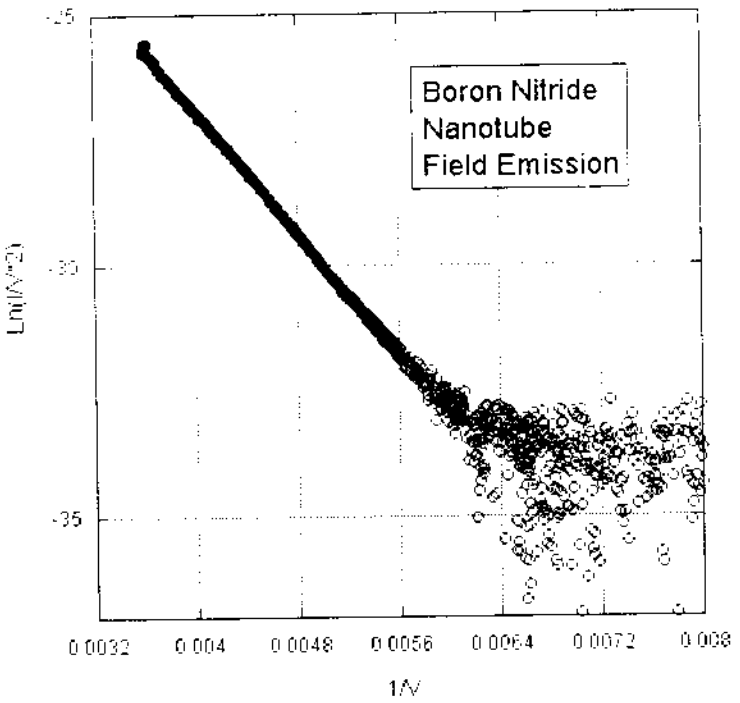

Fig. 11.16. Fowler Nordheim plot of the current-voltage characteristic of field emitting BN nanotubes

11.4 Electron Field Emission from BN Nanotubes

Figure 11.16 shows the results of field emission experiments. The turn-on voltages are approximately 150 volts. This is twice the turn-on voltage measured in control experiments performed using carbon nanotube samples in similar geometries. The current densities, however, are similar in both cases. One notable difference between the field-emission behavior of BN and carbon nanotubes is the current-voltage characteristic. Generally, field emission is characterized using the theory of Fowler and Nordheim [109], which predicts a linear relationship between $\ln(\frac{I}{V^2})$ and V^{-1}. For carbon nanotubes, however, the theory often breaks down, frequently with the current showing saturation at high fields, or two distinct Fowler Nordheim slopes [110]. For the field emission for BN nanotubes we have observed a single slope in the Fowler Nordheim plot. Additionally, carbon nanotubes usually have a noisy, switching behavior most likely associated with gas molecules adsorbed to the tips of the nanotubes [111]. Boron nitride nanotubes, however, show stable field emission with less noise than for typical carbon nanotube samples. This

may have implications for the use of BN nanotubes as stable field emission sources for lighting and flat panel displays.

From the slope of the Fowler Nordheim characteristic, it is possible to extract the work-function of the field emitting material. Following the analysis in [110], it is possible to model the field at the tip of the nanotube by modelling the nanotube tip as a hemisphere. In this model, the field at the tip of the nanotubes can be expressed as

$$E_{\text{loc}} = \frac{V_{\text{applied}}}{(\alpha R_{\text{tip}})}. \tag{11.5}$$

where R_{tip} is the radius of the nanotube tip (in nm) and α is a parameter which captures the details of the geometry of the field emission environment. In this model, the work function (in eV) can then be extracted from the Fowler Nordheim slope (S_{FN}) as

$$\Phi = \left(\frac{-S_{\text{FN}}}{6.8\alpha R_{\text{tip}}}\right)^{2/3}. \tag{11.6}$$

As in [110], we take the enhancement factor to be $\alpha \sim 10$. Over repeated field-emission experiments performed using BN nanotubes inside the TEM, the slope of the Fowler Nordheim characteristic varies from -2600 to -3100. From independent TEM observations, the radius of the tips of the BN nanotubes has been measured to be approximately 1 nm. From these quantities, it is possible to make a rough estimate of the work function in the range of 11–13 eV. This large work function is obviously unphysical, and may indicate that field emission from BN nanotubes does not truly obey the Fowler Nordheim theory. If instead we use the expected work function for hexagonal BN (approximately ~6 eV), (11.6) can be used to calculate the radius of the tip of the field emitting nanotube. From this analysis, $R_{\text{tip}} = 3$ nm.

It is surprising that boron nitride nanotubes can pass any current at all, given that they are wide bandgap semiconductors. Such a counter-intuitive observation deserves careful inspection. We note that the nanotubes in these experiments were observed in the TEM where the are subjected to possible electron beam-induced damage. It may be possible that this beam damage affects the intrinsic properties of the nanotubes, leading to the conductivity. Control experiments, however were performed outside the TEM in a vacuum field-emission setup. In this setup, the nanotubes exhibit field emission with characteristics similar to those observed in the TEM. Therefore, electron beam damage is not essential for field emission from boron nitride nanotubes. The nanotubes are also observed in the TEM to be partly covered with amorphous material from the binder of the conducting epoxy used in the preparation of the nanotube composites. It may be that this material plays some role in the field emission, and future studies using mixtures with different types of binder material, or little to no binder may help address this issue

An additional useful future study would be to look carefully at the current noise during field emission from boron nitride nanotubes. Here, it was observed that BN nanotubes seem to have less noise during field emission, but it would be useful to put this observation on a more solid empirical footing. For instance, the noise frequency spectrum could be carefully measured [11,12] during field emission from both BN nanotubes and from carbon nanotubes (both SWNT and MWNT). Comparison of the noise spectra would show whether BN nanotubes are indeed less noisy than carbon nanotubes, and may even help elucidate the source of the noise.

11.5 Electrical Breakdown and Conduction of BN Nanotubes

The field emission properties of BN nanotubes are surprising given that they are predicted to be wide bandgap semiconductors [6,8], and therefore electrically insulating. To test whether or not individual nanotubes are in fact insulating, the nanotube tips were brought into contact with the gold counter-electrode. For all BN nanotubes observed, there was no conduction at low bias. It is known that often carbon nanotubes can have high contact resistance, but we rule out contact resistance for the case of BN nanotubes, because the voltage can be increased through 10 V with no current or damage to the tube. When this is done with carbon nanotubes, the nanotubes will mechanically fail or burn-out between 2 V and 4 V, even in cases when there is no conductance at low bias. BN nanotubes, therefore, are a good dielectric material up to approximately 10 V. At higher bias voltages, however, some of the BN nanotubes observed pass current, but do so in a reversible, non-destructive manner. Figure 11.17 shows a typical current-voltage relation for individual BN nanotubes. The breakdown generally occurs between 12 V and 25 V, and has a characteristic reminiscent of gas-discharge tubes. In the lower plot of Fig. 11.17, a sharp, reversible turn-on can be seen at 22 V. Such behavior might be characteristic of an avalanche effect leading to breakdown conductivity.

Acknowledgements

We are indebted to M.L. Cohen, P.G. Collins, U. Dahmen, T. Freeman, M.S. Fuhrer, D. Goldhaber-Gordon, W.Q. Han, S.G. Louie, D.K. Owen and E.A. Stach for valuable contributions to the work described here. This research was supported in part by the Director, Office of Energy Research, Office of Basic Energy Sciences, Division of Materials Sciences, of the U.S. Department of Energy under contract No. DE-AC03-76SF00098.

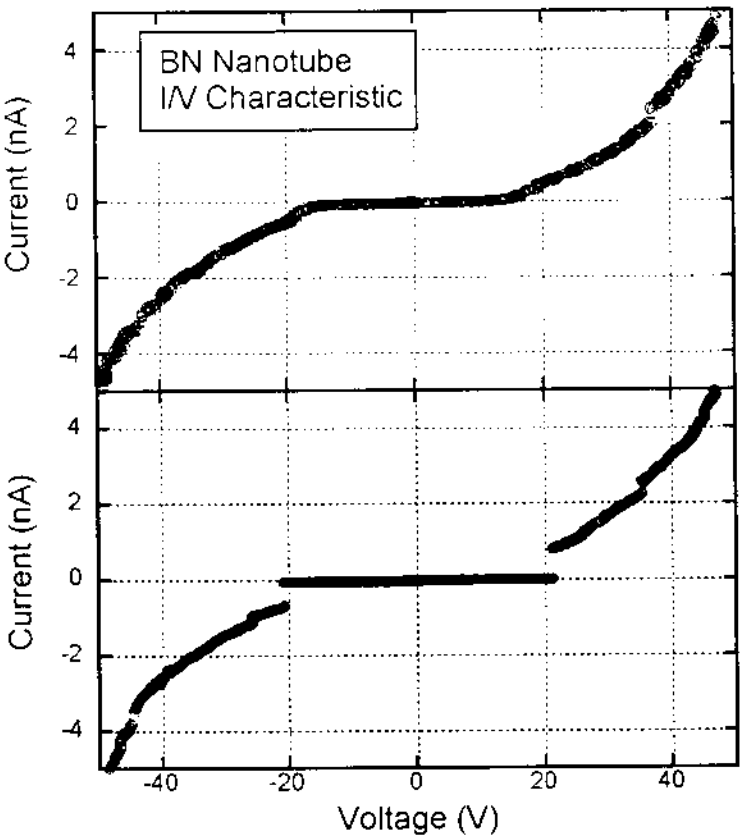

Fig. 11.17. The current-voltage characteristic of typical BN nanotubes under contact conditions. In both cases, the nanotubes protrude from the conducting matrix approximately 400 nm

References

1. S. Iijima: Nature **354**, 56 (1991)
2. N.G. Chopra: Synthesis and Characterization of $B_xC_yN_z$ Nanotubes. PhD Disseratation, University of California, Berkeley (1996)
3. N.G. Chopra, R.J. Luyken, K Cherrey et al: Science **269**, 966 (1995)
4. R.S. Pease: Acta Crystallogr. **5**, 356 (1952)
5. A. Zunger, A. Katzir, A. Halperin: Phys. Rev. B **13**, 5560 (1976)
6. A. Rubio, J.L. Corkill, M.L. Cohen: Phys. Rev. B **49**, 5081 (1994)
7. M. Terauchi, M. Tanaka, T. Matsumoto et al: Journal of Electron Microsc. **47**, 319 (1998)
8. X. Blase, A. Rubio, S.G. Louie et al: Europhys. Lett. **28**, 335 (1994)
9. R.S. Ruoff, D.C. Lorents: Carbon **33**, 925 (1995)

10. J.P. Salvetat, J.M. Bonard, N.H. Thomson et al: Appl. Phys. A **69**, 255 (1999)
11. N.G. Chopra, A. Zettl: Solid State Commun. **105**, 297 (1998)
12. J.P. Lu: Phys. Rev. Lett. **79**, 1297 (1997)
13. D. Sanchez-Portal, E. Artacho, J.M. Soler et al: Phys. Rev. B **59**, 12678 (1999)
14. J.P. Lu: Elastic properties of single and multilayered nanotubes. In: *Fullerenes '96* (Elsevier, Oxford, UK 1997) pp 1049–52
15. E. Hernandez, C. Goze, P. Bernier et al: Phys. Rev. Lett. **80**, 4502 (1998)
16. E. Hernandez, C. Goze, P. Bernier et al: Appl. Phys. A **68**, 287 (1999)
17. N. Yao, V. Lordi: J. Appl. Phys. **84**, 1939 (1998)
18. V.N. Popov, V.E. Van Doren, M. Balkanski: Phys. Rev. B **61**, 3078 (2000)
19. C.F. Cornwell, L.T. Wille: Solid State Commun. **101**, 555 (1997)
20. A. Krishnan , E. Dujardin, T.W. Ebbesen TW et al: Phys. Rev. B **58**, 14013 (1998)
21. M.M.J. Treacy, T.W. Ebbesen, J.M. Gibson: Nature **381**, 678 (1996)
22. J.P. Salvetat, A.J. Kulik, J.M. Bonard et al: Adv. Mater. **11**, 161 (1999)
23. J.P. Salvetat, G.A.D. Briggs, J.M. Bonard et al: Phys. Rev. Lett. **82**, 944 (1999)
24. E.W. Wong, P.E. Sheehan, C.M. Lieber: Science **277**, 1971 (1997)
25. Z.W. Pan, S.S. Xie, L. Lu et al: Appl. Phys. Lett. **74**, 3152 (1999)
26. O. Lourie, H.D. Wagner: J. Mater. Res. **13**, 2418 (1998)
27. P. Poncharal, Z.L. Wang, D. Ugarte et al: Science **283**, 1513 (1999)
28. M.F. Yu, O. Lourie, M.J. Dyer et al: Science **287**, 637 (2000)
29. C. Downs, J. Nugent, P.M. Ajayan et al: Adv. Mater. **11**, 1028 (1999)
30. B.I. Yakobson, C.J. Brabec, J. Bernholc: Phys. Rev. Lett. **76**, 2511 (1996)
31. B.I. Yakobson: Appl. Phys. Lett. **72**, 918 (1998)
32. P. Zhang, P.E. Lammert, V.H. Crespi: Phys. Rev. Lett. **81**, 5346 (1998)
33. M.B. Nardelli, B.I. Yakobson, J. Bernholc: Phys. Rev. Lett. **81**, 4656 (1998)
34. M.B. Nardelli, B.I. Yakobson, J. Bernholc: Phys. Rev. B **57**, R4277 (1998)
35. D.A. Walters, L.M. Ericson, M.J. Casavant et al: Appl. Phys. Lett. **74**, 3803 (1999)
36. G. Binnig, H. Rohrer, C. Gerber et al: Phys. Rev. Lett. **50**, 120 (1983)
37. G. Binnig, H. Rohrer: Scanning tunnelling microscopy. Helv. Phys. Acta **55**, 726 (1982)
38. D.M. Eigler, E.K. Schweizer: Nature **344**, 524 (1990)
39. M.F. Crommie, C.P. Lutz, D.M. Eigler, Science **262**, 218 (1993)
40. M.T. Cuberes, R.R. Schlittler, J.K. Gimzewski: Appl. Phys. Lett. **69**, 3016 (1996)
41. G. Binnig, C.F. Quate, C. Gerber: Phys. Rev. Lett. **56**, 930 (1986)
42. R. Curtis, T. Mitsui, E. Ganz: Rev. Sci. Instrum. **68**, 2790 (1997)
43. Z.L. Wang, P. Poncharal, W.A. de Heer: J. Phys. Chem. Solids **61**, 1025 (2000)
44. Z.L. Wang, P. Poncharal, W.A. de Heer: Microsc. Microanal. **6**, 224 (2000)
45. W.K. Lo, J.C.H. Spence: Ultramicroscopy **48**, 433 (1993)
46. A.M. Minor, J.W. Morris, E.A. Stach: Appl. Phys. Lett. **79**, 1625 (2001)
47. E.A. Stach, T. Freeman, A.M. Minor et al: Microsc. Microanal. **7**, 507 (2001)
48. T.W. Ebbesen, P.M. Ajayan: Nature **358**, 220 (1992)
49. A.G. Rinzler, J. Liu, H. Dai et al: Appl. Phys. A **67**, 29 (1998)

50. P.G. Collins, P. Avouris: Appl. Phys. A **74**, 329 (2002)
51. P.G. Collins, M.S. Arnold, P. Avouris: Science **292**, 706 (2001)
52. P.G. Collins, M. Hersam, M. Arnold et al: Phys. Rev. Lett. **86**, 3128 (2001)
53. M. Freemantle: Chem. Eng. News **74**, 62 (1996)
54. P.J. Britto, K.S.V. Santhanam, P.M. Ajayan: Bioelectroch. Bioener. **41**, 121 (1996)
55. P.G. Collins, A. Zettl, H. Bando et al: Science **278**, 100 (1997)
56. S.J. Tans, R.M. Verschueren, C. Dekker: Nature **393**, 49 (1998)
57. H.Dai H. J.H Hafner, A.G. Rinzler et al: Nature **384**, 147 (1996)
58. W.A. de Heer, A. Chatelain, D. Ugarte: Science **270**, 1179 (1995)
59. J. Kong, H.T. Soh, A.M. Cassell: Nature **395**, 878 (1998)
60. S.C. Tsang, Y.K. Chen, P.J.F. Harris et al: Nature **372**, 159 (1994)
61. J. Cumings, P.G. Collins, A. Zettl: Nature **406**, 586 (2000)
62. S. Frank, P. Poncharal, Z.L. Wang et al: Science **280**, 1744 (1998)
63. A. Bachtold, C. Strunk, J.P. Salvetat et al: Nature **397**, 673 (1999)
64. W. Trimmer: *Micromechanics and MEMS: classic and seminal papers to 1990*. (IEEE Press, New York 1997)
65. S. Iijima, C. Brabec, A. Maiti et al: J Chem Phys **104**, 2089 (1996)
66. H.D. Wagner, O. Lourie, Y. Feldman et al: Appl. Phys. Lett. **72**, 188 (1998)
67. N. Hamada, S. Sawada, A. Oshiyama: Phys. Rev. Lett. **68**, 1579 (1992)
68. R. Saito, M. Fujita, G. Dresselhaus et al: Appl. Phys. Lett. **60**, 2204 (1992)
69. J.C. Charlier, J.P. Michenaud: Phys. Rev. Lett. **70**, 1858 (1993)
70. A. Kolmogorov, V. Crespi: B. Am. Phys. Soc. **45**, 254 (2000)
71. V.H. Crespi, P. Zhang, P.E. Lammert: Sliding, stretching, and tapering: recent structural results for carbon nanotubes. In: *Electronic Properties of Novel Materials Science and Technology of Molecular Nanostructures*, ed by H. Kuzmany, J. Fink, M. Mehring, S. Roth (American Institute of Physics, College Park, MD 1999) pp 364–368
72. L.X. Benedict, N.G. Chopra, M.L. Cohen et al: Chem. Phys. Lett. **286**, 490 (1998)
73. B.N.J. Persson: Surf. Sci. Rep. **33**, 83 (1999)
74. R.W. Carpick, D.F. Ogletree, M. Salmeron: Appl. Phys. Lett. **70**, 1548 (1997)
75. M. Enachescu, R.J.A. Van Den Oetelaar, R.W. Carpick et al: Phys. Rev. Lett. **81**, 1877 (1998)
76. S. Iijima, P.M. Ajayan, T. Ichihashi: Phys. Rev. Lett. **69**, 3100 (1992)
77. N.G. Chopra, L.X. Benedict, V.H. Crespi et al: Nature **377**, 135 (1995)
78. M.R. Falvo, G.J. Clary, R.M. Taylor et al: Nature **389**, 582 (1997)
79. C.T. White, T.N. Todorov: Nature **393**, 240 (1998)
80. A. Bachtold, M.S. Fuhrer, S. Plyasunov et al: Phys. Rev. Lett. **84**, 6082 (2000)
81. A. Javey, J. Guo, Q. Wang et al: Nature **424**, 654 (2003)
82. C. Berger, Y. Yi, Z.L. Wang et al: Appl. Phys. A **74**, 363 (2002)
83. S. Sanvito, Y.K. Kwon, D. Tomanek et al: Phys. Rev. Lett. **84**, 1974 (2000)
84. H. Dai, E.W. Wong, C.M. Lieber: Science **272**, 523 (1996)
85. J. Cumings, A. Zettl: Science **289**, 602 (2000)
86. J.C. Charlier, J.P. Michenaud: Phys. Rev. Lett. **70**, 1858 (1993)
87. M.F. Yu, B.I. Yakobson, R.S. Ruoff: J. Phys. Chem. B **104**, 8764 (2000)
88. J.H. Kim, K.J. Chang: Phys. Rev. B **66**, 155402 (2002)
89. C. Buia, A. Buldum, J.P. Lu: Phys. Rev. B **67**, 113409 (2003)

90. R. Landauer: Philos. Mag. **21**, 863 (1970)
91. D.J. Thouless: Phys. Rev. Lett. **39**, 1167 (1977)
92. G.J. Dolan, D.D. Osheroff: Phys. Rev. Lett. **43**, 721 (1979)
93. D.J. Bishop, D.C. Tsui, R.C. Dynes: Phys. Rev. Lett. **44**, 1153 (1980)
94. M.S. Fuhrer, M.L. Cohen, A. Zettl et al: Solid State Commun. **109**, 105 (1999)
95. Y. Koike, S. Morita, T. Nakanomyo et al: J. Phys. Soc. Jpn. **54**, 713 (1985)
96. P.J. de Pablo, C. Gomez-Navarro, J. Colchero et al: Phys. Rev. Lett. **88**, 036801 (2002)
97. S. Datta: *Electronic transport in mesoscopic systems* (Cambridge University Press, Cambridge New York 1995)
98. N. Apsley, H.P. Hughes: Philos. Mag. **31**, 1327 (1975)
99. S. Roche, F. Triozon, A. Rubio et al: Phys. Lett. A **285**, 94 (2001)
100. P.A. Lee, T.V. Ramakrishnan: Rev. Mod. Phys. **57**, 287 (1985)
101. Z. Yao, C.L. Kane, C. Dekker: Phys. Rev. Lett. **84**, 2941 (2000)
102. J. Hone: Phonons and thermal properties of carbon nanotubes. In: *Carbon Nanotubes: Synthesis, Structure, Properties, and Applications*, ed by M.S. Dresselhaus, G. Dresselhaus, P. Avouris (Springer Verlag, Berlin 2001) pp 273–286
103. F. Leonard, J. Tersoff: Phys. Rev. Lett. **83**, 5174 (1999)
104. N. de Jonge, Y. Lamy, K. Schoots et al: Nature **420**, 393 (2002)
105. J. Clarke: Physica B & C **126**, 441 (1984)
106. R.V. Jones: P.I. Electr. Eng. **117**, 1185 (1970)
107. J. Cumings, A. Zettl: Chem. Phys. Lett. **316**, 211 (2000)
108. K.B. Shelimov, R.O. Esenaliev, A.G. Rinzler et al: Chem. Phys. Lett. **282**, 429 (1998)
109. R.H. Fowler, L. Nordheim: Proc. R. Soc. Lon. Ser. A **119**, 173 (1928)
110. P.G. Collins, A. Zettl: Phys. Rev. B **55**, 9391 (1997)
111. K.A. Dean, B.R. Chalamala: Appl. Phys. Lett. **76**, 375 (2000)
112. P.G. Collins, M.S. Fuhrer, A. Zettl: Appl. Phys. Lett. **76**, 894 (2000)